J. Fluid Mech. (2002), *vol.* 464, *pp.* 113–136. © 2002 Cambridge University Press
DOI: 10.1017/S0022112002008844 Printed in the United Kingdom

PLIF flow visualization and measurements of the Richtmyer–Meshkov instability of an air/SF$_6$ interface

By **B. D. COLLINS AND J. W. JACOBS**
University of Arizona, Tucson, AZ 85721, USA

(Received 21 May 2000 and in revised form 4 February 2002)

Investigations of the Richtmyer–Meshkov instability carried out in shock tubes have traditionally used membranes to separate the two gases. The use of membranes, in addition to introducing other experimental difficulties, impedes the use of advanced visualization techniques such as planar laser-induced fluorescence (PLIF). Jones & Jacobs (1997) recently developed a new technique by which a perturbed, membrane-free gas–gas interface can be created in a shock tube. The gases enter the shock tube from opposite ends and exit through two small slots on opposite sides of the test section, forming a stagnation point flow at the interface location. A gentle rocking motion of the shock tube then provides the initial perturbation in the form of a standing wave. The original investigation using this technique utilized dense fog seeding for visualization, which allowed large-scale effects to be observed, but was incapable of resolving smaller-scale features. PLIF visualization is used in the present study to investigate the instability generated by two incident shock strengths ($M_s = 1.11$ and 1.21), yielding very clear digital images of the flow. Early-time growth rate measurements obtained from these experiments are found to be in excellent agreement with incompressible linear stability theory (appropriately adjusted for a diffuse interface). Very good agreement is also found between the late-time amplitude measurements and the nonlinear models of Zhang & Sohn (1997) and Sadot *et al.* (1998). Comparison of images from the $M_s = 1.11$ and 1.21 sequences reveals a significant increase in the amount of turbulent mixing in the higher-Mach-number experiments, suggesting that a mixing transition has occurred.

1. Introduction

Richtmyer–Meshkov (RM) instability occurs when an interface separating fluids of different densities is impulsively accelerated, such as by the passage of a shock wave over an interface between two dissimilar gases (Richtmyer 1960; Meshkov 1969). RM instability is closely related to the well-known Rayleigh–Taylor instability that develops on an interface under constant acceleration such as produced by the suspension of a heavy fluid over a lighter one in the Earth's gravitational field (Rayleigh 1883; Taylor 1950). Therefore, RM instability is often referred to as impulsive or shock-induced Rayleigh–Taylor instability.

The presence of RM instability has been found to be of importance to a variety of scientific disciplines. In astrophysics, significant fluid mixing in a supernova has been directly attributed to RM instability (Arnett *et al.* 1989). In inertial confinement fusion the RM instability of the impulsively accelerated shell containing the deuterium-tritium fuel limits the compression of the fuel. Thus, RM instability represents a significant obstacle to achieving a productive fusion reaction (Lindl, McCrory & Campbell 1992). The fundamental mechanism in RM instability has also been considered to be of importance to enhancing mixing in supersonic combustion (Yang, Kubota & Zukoski 1993).

Taylor (1950) was first to study the growth of perturbations to a flat interface between two fluids of different densities under constant acceleration (gravity) using linear stability theory. Richtmyer (1960), a decade later, used Taylor's results as the basis for his similar analysis of RM instability in which he modelled the shock interaction with an interface as the impulsive acceleration of two incompressible fluids. Thus, Richtmyer followed Taylor's formulation, modelling gravity as a Dirac delta function, and found the growth rate of the impulsively accelerated instability to be given by

$$\frac{\mathrm{d}a}{\mathrm{d}t} = kAVa_0, \tag{1}$$

where V is the interface velocity, $k = 2\pi/\lambda$ is the wavenumber, a is the amplitude (with a_0 being its initial value) and A is the Atwood number defined as

$$A = \frac{\rho_2 - \rho_1}{\rho_2 + \rho_1},$$

where ρ_1 and ρ_2 are the densities of the gases above and below the interface. Unlike Rayleigh–Taylor instability, which grows exponentially with time when the amplitude is sufficiently small and occurs only when the acceleration is directed from the lighter fluid into the heavier one, RM instability grows at a constant rate in the small-amplitude limit and will develop regardless of the direction that the incident shock travels. When the shock wave passes from the lighter into the heavier fluid the impulsive acceleration has similar orientation to that producing Rayleigh–Taylor instability. Thus the amplitude increases at a constant rate. Conversely, when the shock wave is oppositely directed the amplitude first decreases until it passes through zero, after which it emerges as a growing waveform that has been shifted in phase by 180°. Note that Richtmyer only considered the light-to-heavy configuration even though his derived result (1) applies equally to both. The heavy-to-light configuration was subsequently introduced by Meshkov (1969).

The linear growth stage described by Richtmyer's result lasts as long as the perturbation amplitude is sufficiently small (typically as long as $ka < 1$). When the amplitude becomes comparable to the wavelength, the growth rate decreases owing to the influence of the nonlinearity of the governing equations. The effects of weak nonlinearity can be incorporated by developing a solution in the form of an asymptotic expansion using the perturbation amplitude as the small parameter (Haan 1991). These solutions, however, have the weakness that when truncated they produce results that quickly diverge from the exact solution when the amplitude reaches moderate size. Zhang & Sohn (1997) have found a solution to this problem by posing their series solution as a Padé approximant which significantly extends its validity. One shortcoming of Zhang & Sohn's solution is that it does not possess the generally accepted asymptotic behaviour that the growth rate decays as $1/t$ as time, t, approaches infinity. This weakness has been addressed by Sadot *et al.* (1998) who present a model that captures the initial weakly nonlinear behaviour yet also provides the correct late-time asymptotic form.

The impulsive acceleration in RM instability is generally produced by the passage of a shock wave over the interface. Thus the most common method for generating

RM instability in the laboratory is to create a boundary between two gases in a shock tube. Early shock-tube-driven RM experiments utilized a physical barrier to initially separate the two gases in order to prevent their mixing. However, this barrier subsequently introduced other problems. The earliest such method, used by Meshkov and others (Aleshin *et al.* 1988; Vassilenko *et al.* 1992; Benjamin 1992), employed a thin membrane pre-shaped into a sinusoid and placed between the two gases to separate them and provide the initial perturbation. This membrane is shattered by the incident shock wave. However, the pieces of the membrane become incorporated into the fluid flow, potentially affecting the development of the instability. The presence of the membrane fragments in the flow also impedes the use of advanced fluid visualization techniques such as planar laser-induced fluorescence (PLIF) (Jacobs 1993), planar Rayleigh scattering (Budzinski, Benjamin & Jacobs 1994) and particle image velocimetry (Rightley *et al.* 1999). Furthermore, this method often produces initial growth rate measurements that are significantly less than Richtmyer's theoretical prediction, typically by a factor of two or more. Another earlier method for interface formation uses a thin plate to separate the fluids (Brouilette & Sturtevant 1994; Cavailler *et al.* 1990; Bonazza & Sturtevant 1996), the wake of which, when extracted prior to shock tube firing, provides a pseudo-sinusoidal interface perturbation. The results of these experiments are limited by the fact that the initial perturbation is uncontrolled, non-uniform and often irreproducible. As is characteristic of all fluid instabilities, the initial state of the system dictates future behaviour, hence any variation in initial conditions makes it difficult to compare experimental results from experiment to experiment. The interfaces created by this method are also very diffuse, having thicknesses equalling or exceeding the perturbation wavelength, which significantly slows instability growth. More recently, experiments studying the RM instability of two nearby interfaces utilizing a 'gas curtain' (Jacobs *et al.* 1993, 1995; Budzinski *et al.* 1994; Rightley *et al.* 1999) have successfully produced membrane-less experiments which utilize advanced diagnostic techniques. However, the dynamics of the two-interface system are significantly more complex than the more fundamental and practically relevant single-interface configuration.

A novel solution to the problem of interface generation and perturbation was devised by Jones & Jacobs (1997). A vertical shock tube was manufactured with small horizontal slots located on two opposite walls. The gases entered the shock tube from opposite ends of the driven section and exited through the slots, forming a stagnation point flow at the interface location. A reproducible perturbation was then given to the interface by gently oscillating the shock tube at the appropriate frequency, generating a standing wave. This investigation made use of a dense fog seeded into one of the gases to visualize the flow. The dense fog allowed large-scale effects to be observed, but obscured the smaller-scale features of the flow. This shortcoming has prompted the desire to implement an alternative imaging technique to allow a more detailed examination of the instability. Low-density fog seeding has been shown to be effective in visualizing small-scale features in gas curtain experiments (Rightley *et al.* 1999). However, even a fog consisting of sub-micron size droplets diffuses at a rate orders of magnitude less than the gas constituents which it is intended to track. In contrast, PLIF utilizes a fluorescent gas to track gas constituents. Thus it is inherently better suited as a diagnostic for mixing. When properly corrected, the captured PLIF images have pixel values that reflect the concentration of the fluorescing tracer, and hence the concentration of the traced gas, which can be used to quantify the degree of mixing that has occurred.

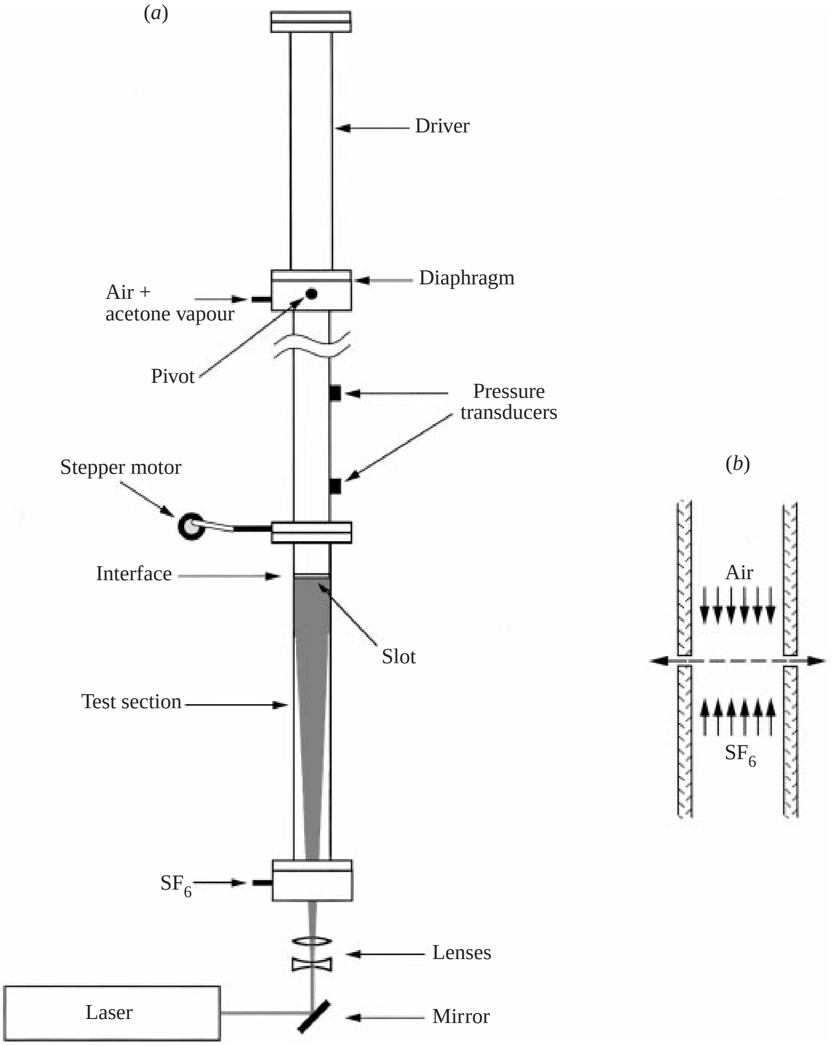

FIGURE 1. The shock tube and PLIF system. SF_6 and an air–acetone mixture flow into the shock tube from plenums located below and above the test section. The stagnation point flow at the slot location creates the interface (*b*), which is given a sinusoidal perturbation by rocking the shock tube using a stepper motor and crank mechanism. Pressure transducers located above the test section sense the shock wave and trigger the laser pulse which produces a light sheet that illuminates the air–acetone mixture.

2. Experimental setup

The experiments utilize a vertical shock tube (figure 1*a*) which is 4.3 m long and has a 1 m long, 10.2 cm diameter driver, and a 3.3 m long driven section with a 8.9 cm square cross-section. The driver is made of glass fibre wound round epoxy pipe, and the upper portion of the driven section is made of extruded fibreglass square structural tubing. Three walls of the test section are made of flat black anodized aluminium while the fourth wall is transparent acrylic sheet to allow full optical access for flow visualization.

An interface is formed in the shock tube test section (Jones & Jacobs 1997) by introducing a relatively light gas (air) through a plenum located at the top of the driven section and a heavier gas (SF_6), through a similar plenum located at the bottom of the test section. The gases meet and are allowed to exit the shock tube through slots located near the upper end of the test section, thus forming a stagnation point flow at the interface location (figure 1*b*). The thickness of the resulting interface is a function of the flow rates of the two gases. By examining digital images captured over a wide range of flow rates, it was determined that equal flow rates of $6\,\mathrm{l\,min^{-1}}$ were optimal in that a relatively thin (≈ 5 mm) interface was obtained at minimal gas expenditure. A nominally sinusoidal perturbation is given to the resulting interface by gently rocking the shock tube on its pivot pins located near the top of the driven section using a small crank driven by a stepper motor running at the appropriate frequency to create a standing wave. A 0.5 mm oscillation amplitude was used in this study which generated a wave amplitude of approximately 2 mm. While it is possible to generate larger initial perturbation amplitudes, it was found that excessively large shock tube oscillations produced an asymmetrical interface. Thus smaller-amplitude perturbations, producing waveforms more sinusoidal in shape, were used. The initial conditions in this experiment are not quiescent. The initial perturbation is that of an oscillating standing wave superimposed onto the constant flow of the two gases toward the interface. The 3.6 Hz rocking motion produces sinusoidal wave motion with a velocity amplitude of $5\,\mathrm{cm\,s^{-1}}$. However, the firing of the shock tube is synchronized with the wave motion such that this velocity is at its minimum. Therefore, the oscillatory velocity perturbation is negligible at the time of shock interaction. The working gases flow down the tube at a velocity of $1.2\,\mathrm{cm\,s^{-1}}$ and exit through the slots. Thus, the flow field near the interface resembles a stagnation point flow. However, it should be stressed that the velocity of this motion is negligible when compared with that resulting from shock interaction which is at least $4\,\mathrm{m\,s^{-1}}$.

PLIF flow visualization was implemented in these experiments by seeding the light gas with acetone vapour. Acetone is relatively harmless, inexpensive, readily available and fluoresces in the visible spectrum when illuminated with light in the 225–320 nm range making it an excellent candidate for use as a tracer in this application (Lozano, Yip & Hanson 1992). However, because the excitation wavelengths lie in the UV spectrum, it was necessary to use a fused silica window to allow the laser light to enter the shock tube. Seeding was accomplished by passing the air flow through a fritted glass cylinder submerged in a canister filled with acetone. Two of these acetone canisters were used in series, the first of which was heated to ensure super-saturation at room temperature. The second canister, at room temperature, served to recover some of the excess acetone and partially cool the gas mixture, which subsequently flowed through copper coils submerged in a cold water bath at constant temperature. The seeded mixture exiting the coils was then of reproducible density, and slightly undersaturated at room temperature, helping to ensure experimental consistency while avoiding potential equipment damage due to unwanted acetone condensation. The resulting air–acetone mixture was thus entirely free of liquid-phase acetone and had an acetone volume fraction of approximately 25%.

The fourth harmonic (266 nm) of a pulsed Nd:YAG laser was used to illuminate the air–acetone mixture for PLIF visualization. The laser's 70 mJ output pulse was passed through circular and cylindrical lenses and reflected upward through the fused silica window at the lower end of the shock tube. The result was a diverging light sheet that momentarily illuminated a thin (≈ 1 mm) cross-section of the air–acetone mixture. The brief fluorescence of the acetone tracer was captured on a thermoelectrically cooled CCD camera with a f/1.2 50 mm lens. The slow, 7 s, cycle time of the cooled

CCD camera, and the 10 Hz pulse rate of the laser both limited data acquisition to one image per shock-tube firing.

The puncturing of a polypropylene diaphragm placed between the pressurized driver and driven section of the shock tube generated a weak shock wave that travelled down the tube and through the perturbed interface, initiating the onset of the instability. The coordination of the output of the pulsed laser with the firing of the shock tube was necessary in order to capture an image of the interface as it travelled down the test section and past the camera. Electronic timing circuitry was built to fire the laser flashlamp at the appropriate frequency, sense the closing of a manual firing switch, then wait for the appropriate time in the shaking cycle of the shock tube before closing the circuit that powers the solenoid responsible for puncturing the diaphragm. Two pressure transducers, mounted on the wall of the shock-tube driven section, served the dual purpose of triggering a digital delay generator that subsequently triggered the laser's Q-switch, and also triggering separate channels of a digital timer that was used to measure the shock speed (and hence the Mach number) and calculate its time of arrival at the interface. In this way, the development time of the instability could be chosen *a priori* (within about 10 μs) and the camera could be placed to view the appropriate portion of the test section to capture the fluorescent signal from the passing interface.

3. Image correction

Figure 2(*a*) shows an uncorrected raw PLIF image as acquired by the CCD camera. The instability is clearly evident in this image. However, the effects of non-uniform laser illumination and Beer's law attenuation are also readily apparent. It is possible to improve the raw images considerably by correcting for laser divergence, attenuation, and laser beam profile to yield images with brightness values that more closely represent the concentration of the PLIF tracer, and hence provide an approximation to the concentration of the traced gas. This was accomplished using a correction routine that marched along individual light rays integrating Beer's law.

The differential form of the Beer–Lambert law is

$$\mathrm{d}I = -\varepsilon C_0 \xi I \,\mathrm{d}s, \tag{2}$$

where I is the light ray intensity, ε is the extinction coefficient, C_0 is the acetone concentration far above the interface, $\xi = C/C_0$ is the normalized acetone concentration and s is distance along a light ray. For any given pixel in an image, the recorded intensity value, i, is given by

$$i = g C_0 \xi I, \tag{3}$$

where g is a constant associated with the collection efficiency of the camera and lens system. Combining (2) and (3) and integrating along a light ray gives

$$I - I_0 = -\frac{\varepsilon}{g}\int i \,\mathrm{d}s. \tag{4}$$

Finally, combining (3) and (4), yields

$$\xi = \frac{i}{i_0 - \varepsilon C_0 \displaystyle\int i \,\mathrm{d}s}, \tag{5}$$

which gives the acetone concentration as a function of other measurable quantities.

Equation (5) was used to obtain the tracer concentration field where the integration

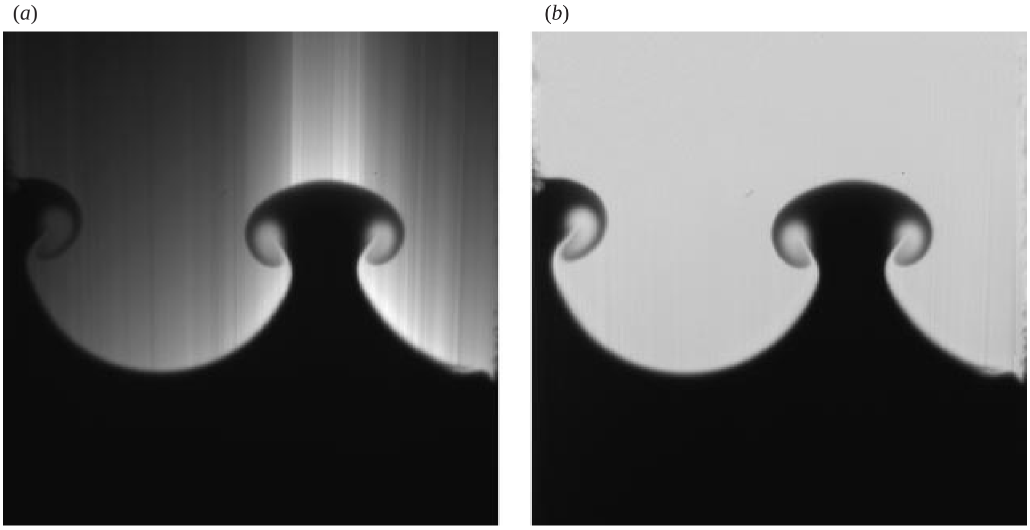

FIGURE 2. The uncorrected image in (*a*) is the raw data acquired by the camera, the brightness of which is a function of the acetone concentration and available laser light. Beer's law attenuation is evident, as is the Gaussian-like laser sheet intensity distribution. The corrected image in (*b*) has brightness that is proportional to the acetone concentration, hence brightness represents the presence of the lighter gas mixture.

was carried out along light rays starting from the top of the image, which was assumed to contain uniformly seeded gas of concentration, $\xi = 1$. The ray paths were determined by first identifying the coordinates of two points along each of several different rays spaced across the diverging laser sheet. From these points the path of the ray that passes through an arbitrary pixel can be calculated. Thus for any given pixel an array of values representing the recorded intensity $i(s)$ along the light ray that illuminates that pixel can be assembled. Having assembled such a vector for each pixel in the image, these vectors are then integrated to yield the tracer concentration field. The product, εC_0, was found by fitting an exponential function to ray vectors above the interface, where the acetone concentration is assumed to be uniform. Figure 2(*b*) shows the corrected version of figure 2(*a*) where now the pixel intensity represents the actual acetone seeding concentration.

4. Results and discussion

Experiments were conducted for two incident shock wave Mach numbers, $M_s = 1.11 \pm 0.01$ and 1.21 ± 0.02, and images were captured at times up to 11 ms after shock arrival, with several images captured at each time level. All experiments had a pre-shock Atwood number of 0.604. Figure 3 is a wave diagram of the $M_s = 1.11$ experiments and figure 4 is an equivalent diagram for the $M_s = 1.21$ experiments. Note that a weak expansion wave is generated by the incident shock when it passes over the slots. This interaction subsequently results in a reduction in the interface velocity and the strength of the transmitted shock wave. In both conditions the interface is reaccelerated at $t \approx 6$ ms by a combination of the reflected expansion wave generated by the diaphragm rupture and the reflected incident shock wave. However, in both conditions it is the reflected expansion that arrives at the interface first.

Figures 5 and 6 contain representative images from the experiments conducted

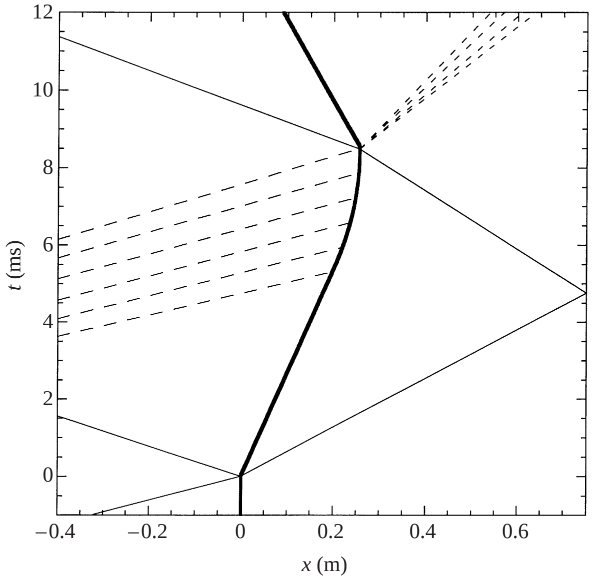

FIGURE 3. An x, t diagram for the $M_s = 1.11$ experiments.

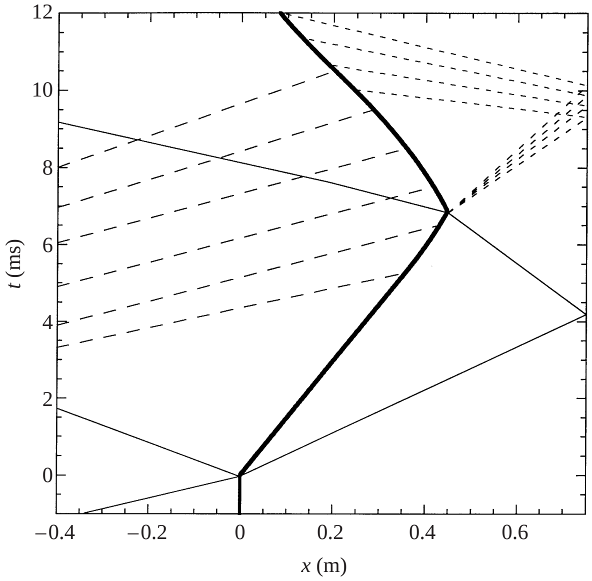

FIGURE 4. An x, t diagram for the $M_s = 1.21$ experiments.

at $M_s = 1.11$ and 1.21, respectively, arranged to form a time sequence. The images in these sequences are displayed in false colour with red representing the lowest fluorescent intensity and blue the highest. As previously mentioned, only one image can be acquired per experiment, consequently figures 5 and 6 were assembled from 18 and 20 separate experiments, respectively. The first image in figure 5 was taken slightly before the arrival of the shock wave and the second image was taken immediately after shock interaction (at $t = 18\,\mu s$). Note that at this time the shock wave is just 3 mm below the interface and would be visible in the picture if it were not for the fact that the lower heavy gas contains no tracer. Both the initial amplitude and interface thickness of the pre-shock perturbation are noticeably reduced by the compression of the incident shock wave. After the interface is impulsively accelerated, the instability grows quickly and remains approximately sinusoidal in shape. However, as the amplitude becomes similar in size to the wavelength, the shape develops asymmetry, with the wave crests thinning into spikes and the troughs broadening into bubbles. Note that the asymmetry of the bubbles and spikes in these experiments is due to the relatively large Atwood number ($A \approx 0.6$). Other Richtmyer–Meshkov and Rayleigh–Taylor investigations (Jacobs & Niederhaus 1997; Waddell, Niederhaus & Jacobs 2001) using much lower-Atwood-number fluid systems exhibit nearly perfect top-to-bottom symmetry.

Still later in time ($t \approx 4\,\text{ms}$) cusps appear that develop into mushroom-shaped structures, indicating the formation of vortices. Note that vorticity is generated in this flow by the interaction of the pressure gradient (∇p) in the shock wave with the density gradient ($\nabla \rho$) at the fluid interface, as described by the two-dimensional vorticity equation,

$$\rho \frac{\mathrm{D}}{\mathrm{D}t}\left(\frac{\boldsymbol{\omega}}{\rho}\right) = \frac{1}{\rho^2}\nabla \rho \times \nabla p,$$

where $\boldsymbol{\omega}$ is the vorticity vector, which in this case is directed normal to the plane of motion. This baroclinically generated vorticity is initially deposited in an approximately sinusoidal distribution. However, as the instability develops it coalesces into vortices via the mechanism that produces Kelvin–Helmholtz instability (Zabusky 1999). Note that the interface begins its evolution in a relatively diffuse state. However, with time, the straining motion induced by the vortex rollup stretches the interface, producing a sharper density distribution except in the regions near the vortex centres. In these regions the motion that produces the coalescence of the vorticity transports mixed interface fluid, depositing it, along with the vorticity, in the vortex cores.

The interface experiences reacceleration in the opposite direction produced by the interaction with the expansion wave that was generated by the diaphragm rupture and had subsequently reflected off the top of the driver. The velocity change imparted by this second interaction is approximately the same as that generated by the shock. However, because the interface amplitude is much larger (and consequently that the surface slopes are larger) in the second interaction, significantly more vorticity is generated (Kotelnikov, Ray & Zabusky 2000). Most of this new vorticity has the opposite sense to that originally deposited (its appearance being most evident in the stems of the mushrooms, figure 5*i*). As a result it causes the interface to invert and change rapidly (figure 5*j–o*). The interface is accelerated a third time in this sequence by the incident shock wave that has reflected off the bottom of the shock tube. This shock passes over the interface, depositing new vorticity and producing a much more complex and possibly turbulent flow.

The sequence produced by interaction with the $M_s = 1.21$ (figure 6) shock develops similarly to $M_s = 1.11$ sequence. The principal difference between the two is that the $M_s = 1.21$ sequence receives an impulsive acceleration that is approximately twice as large as that of the $M_s = 1.11$ sequence. Thus, since it is the velocity change that determines the instability growth rate, as given by Richtmyer's result (1), the development of the instability occurs approximately twice as fast. However, the arrival of the expansion (and thus the beginning of reacceleration) occurs at approximately the same time in both sequences. Thus, because the $M_s = 1.21$ sequence develops at a much faster rate, it is much further developed at the time that the expansion wave

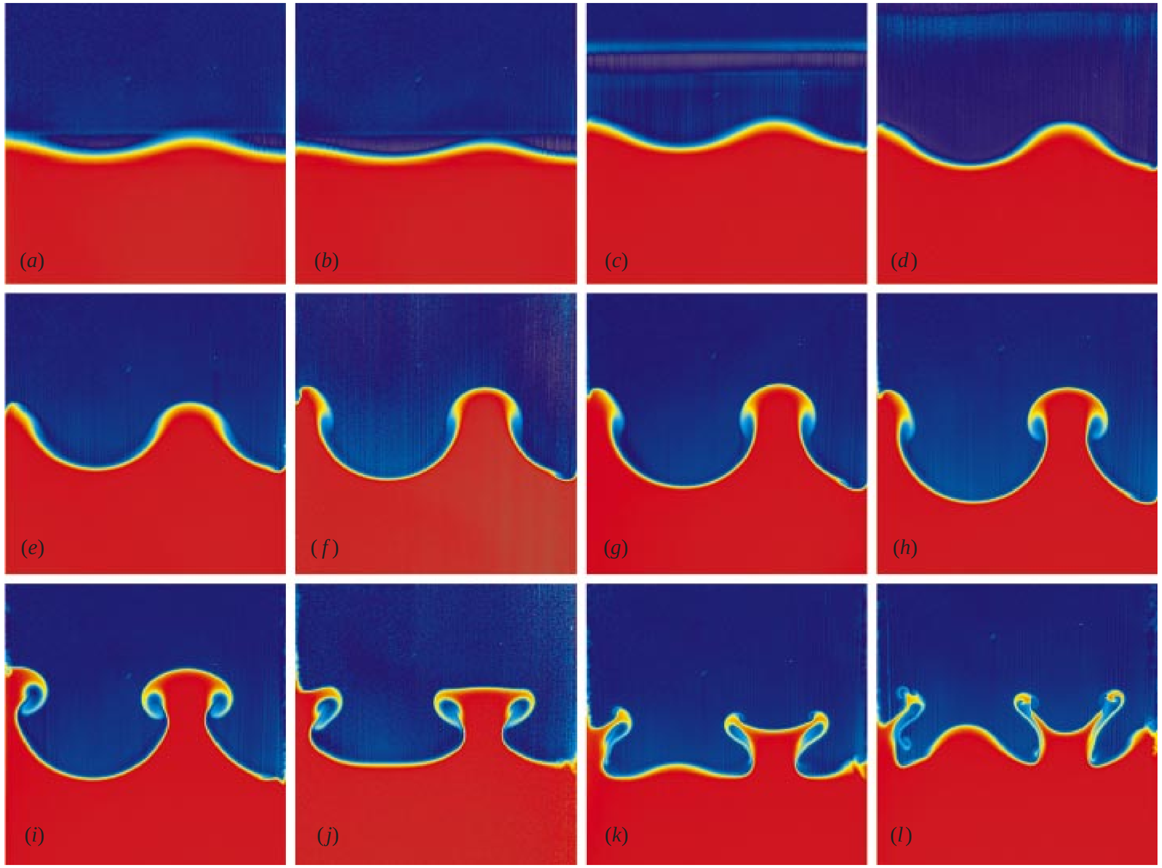

FIGURE 5(*a*–*l*). For caption see facing page.

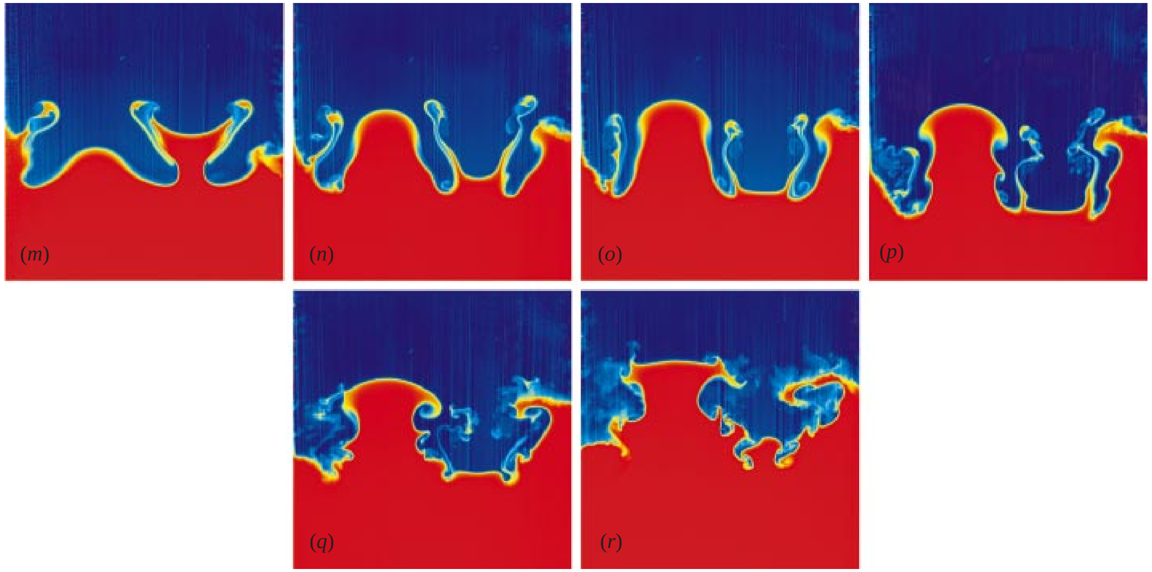

FIGURE 5. Corrected PLIF images assembled to form a time sequence of the instability resulting from shock-acceleration by an $M_s = 1.11$ incident shock wave. Frame (*a*) was taken slightly before the arrival of the shock wave. Times relative to the shock wave arrival for the other images are: (*b*) 0.018 ms, (*c*) 0.607 ms, (*d*) 1.212 ms, (*e*) 2.207 ms, (*f*) 3.217 ms, (*g*) 4.215 ms, (*h*) 5.204 ms, (*i*) 6.221 ms, (*j*) 7.026 ms, (*k*) 7.546 ms, (*l*) 8.027 ms, (*m*) 8.535 ms, (*n*) 8.804 ms, (*o*) 9.054 ms, (*p*) 9.555 ms, (*q*) 10.053 ms, (*r*) 10.558 ms.

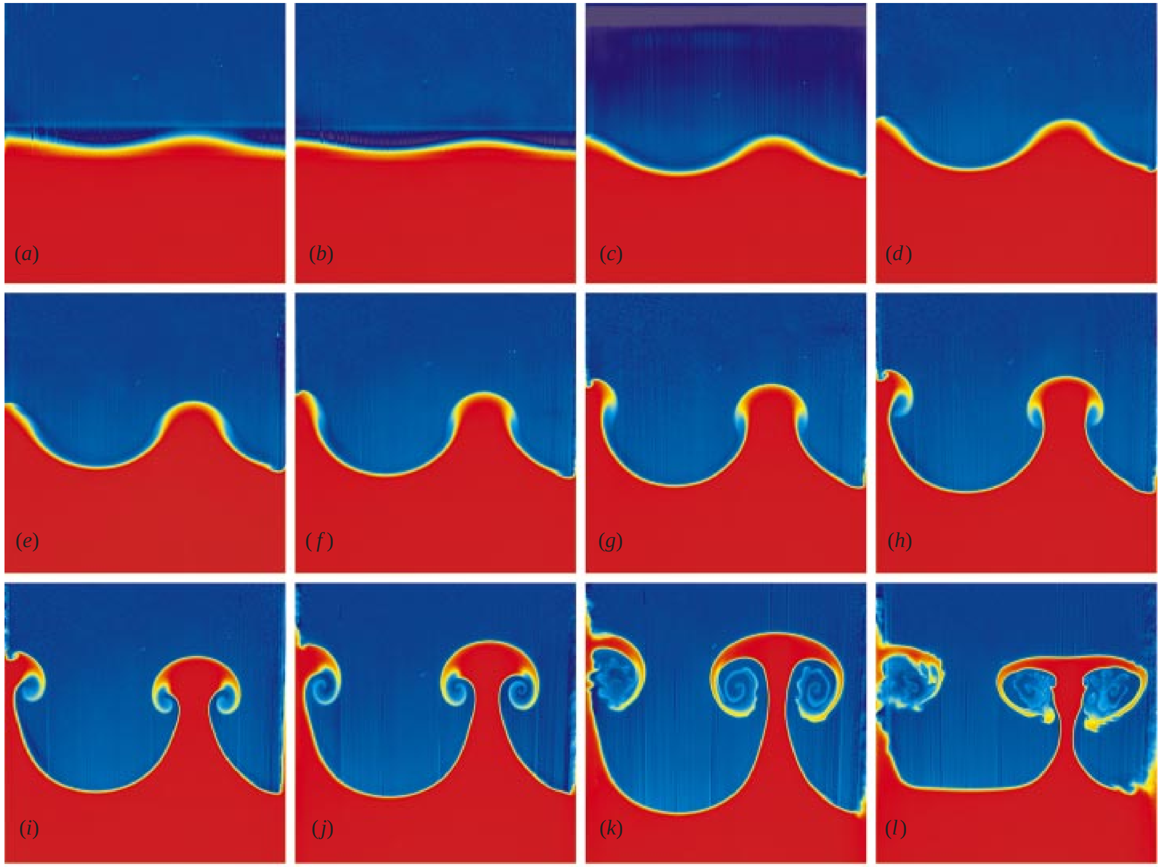

FIGURE 6(*a*–*l*). For caption see facing page.

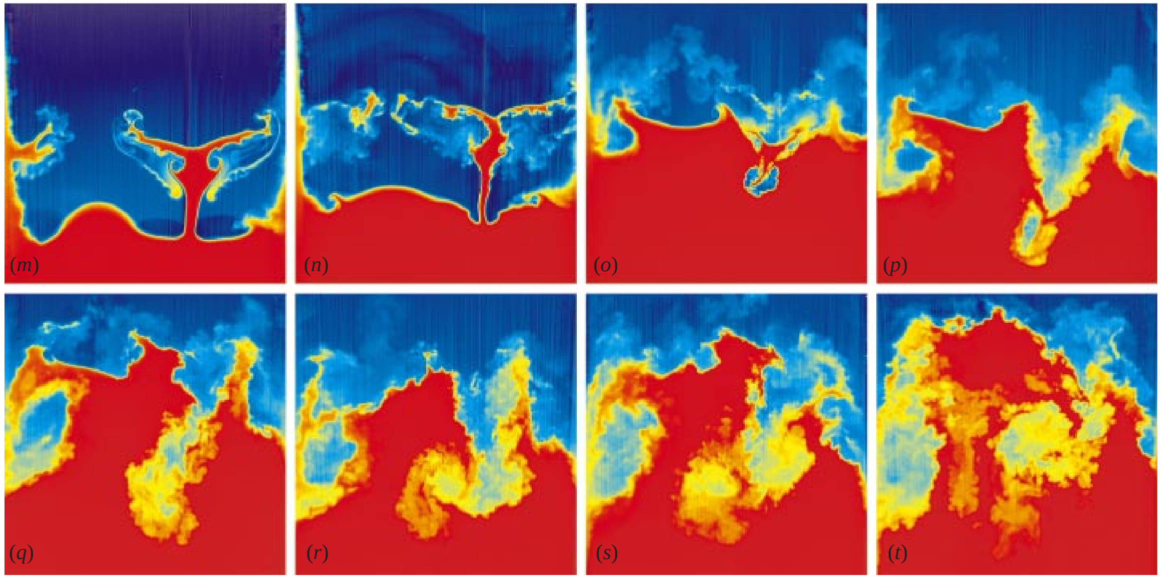

FIGURE 6. Corrected PLIF images assembled to form a time sequence of the instability resulting from shock-acceleration by an $M_s = 1.21$ incident shock wave. Frame (*a*) was taken slightly before the arrival of the shock wave. Times relative to the shock wave arrival for the other images are: (*b*) 0.023 ms, (*c*) 0.632 ms, (*d*) 1.031 ms, (*e*) 1.478 ms, (*f*) 2.014 ms, (*g*) 2.502 ms, (*h*) 3.011 ms, (*i*) 4.009 ms, (*j*) 5.015 ms, (*k*) 6.006 ms, (*l*) 7.005 ms, (*m*) 7.781 ms, (*n*) 8.009 ms, (*o*) 8.499 ms, (*p*) 9.021 ms, (*q*) 9.524 ms, (*r*) 10.020 ms, (*s*) 10.519 ms, (*t*) 11.001 ms.

arrives. As a result, the vortices observed in figure 6 are much further developed, showing much more rollup, than their counterparts in figure 5. In addition, the beginning of a secondary instability in the vortex cores is clearly evident in figure 6(k). Note that a similar instability has been observed in shock-accelerated heavy gas cylinders (Jacobs 1993) and in incompressible RM experiments (Niederhaus 2000).

There are other noticeable differences between the $M_s = 1.11$ and $M_s = 1.21$ sequences besides their relative rates of development. The reflected expansion arrives in the $M_s = 1.21$ sequence at approximately 5 ms and the reflected shock can be observed to be passing over the interface in figure 6(m). These two sources add to produce a dramatic increase in complexity similar to that observed in the $M_s = 1.11$ sequence. However the transition is much more pronounced in figure 6. The later images of figure 5 show a very complex interface shape indicating the beginnings of turbulence. However there is very little mixed fluid present. The images taken at the latest times in figure 6 show a substantial increase in the amount mixed fluid, giving little doubt that a turbulent flow has been achieved.

The increase in the amount of mixed fluid produced in the higher Mach number experiments is further illustrated in figure 7 which is a comparison of the histograms of the concentration data of the last image from each of the displayed $M_s = 1.11$ and $M_s = 1.21$ sequences (figures 5r and 6t). The histogram of figure 5(r) shows two large spikes corresponding to the two pure constituents with very little mixed fluid in between. In contrast, the histogram of figure 6(t) shows a significant increase in the number of pixels with concentrations between the two extremes indicating the substantial presence of mixed fluid. The amount of mixed fluid is often quantified in studies of mixing in turbulent shear layers by the mixed fluid thickness (Koochesfahani & Dimotakis 1986) defined as

$$h_m = \frac{1}{x_2 - x_1} \int_{y_1}^{y_2} \int_{x_1}^{x_2} \xi_m(\varepsilon)\, \mathrm{d}x\, \mathrm{d}y,$$

where

$$h_m(\varepsilon) = \begin{cases} 1 & \text{for } \varepsilon < \xi < 1 - \varepsilon \\ 0 & \text{otherwise,} \end{cases}$$

and ε is representative of the signal-to-noise ratio of the concentration measurements. Figure 8 shows the development of h_m for the data sequences of figures 5 and 6 where $\varepsilon = 0.1$ and the domain of integration is the field of view in these images. One can see that h_m is very similar for the two sequences until interaction with the reflected waves at $t \approx 6$ ms. Afterwards, the $M_s = 1.21$ experiments show a very rapid growth in h_m while in the $M_s = 1.11$ sequence h_m continues to grow at a rate approximately equal to its initial value. Thus, despite the fact that the $M_s = 1.11$ instability has developed some of the characteristics of turbulence, such as a random-like appearance and increased sensitivity to initial conditions, the rate of production of mixed fluid has not significantly changed, indicating that turbulence has not yet been achieved. The changes observed in the comparisons of figures 5 and 6 are very similar to those observed in studies of turbulent shear layers when PLIF images taken above and below the mixing transition are compared (Breidenthal 1981; Koochesfahani & Dimotakis 1986; Dimotakis 2000). Thus, the increase in the incident shock Mach number appears to have resulted in a mixing transition in this flow. Note that Rightley *et al.* (1999) have observed a similar mixing transition in shock-accelerated gas curtain experiments. However, it should be stressed that it is also possible that the $M_s = 1.11$ condition may eventually experience a transition to turbulence given sufficient time to evolve.

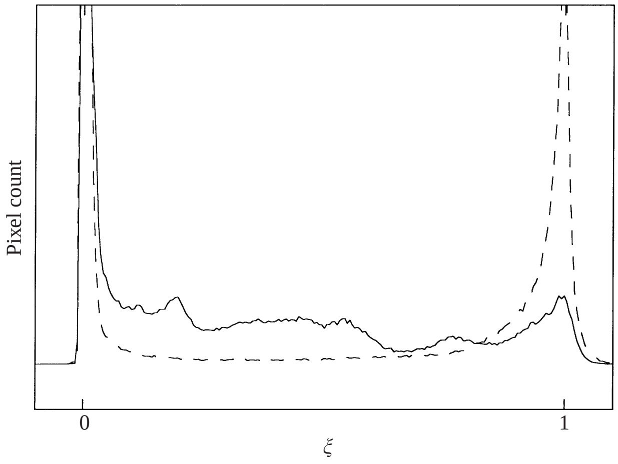

FIGURE 7. A comparison of the histograms of acetone concentration from images 5(*r*) and 6(*t*): - - -, $M_s = 1.11$; ——, $M_s = 1.21$.

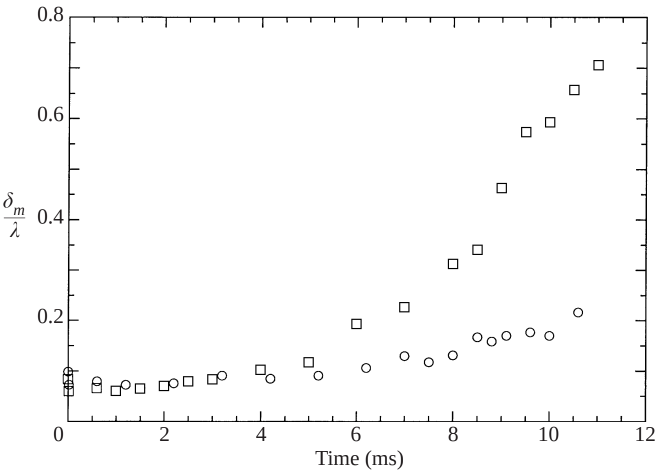

FIGURE 8. The development of the mixed fluid thickness for the data of figures 5 and 6: ○, $M_s = 1.11$; □, $M_s = 1.21$.

4.1. *Repeatability*

The experiments were designed to maximize repeatability. The most important part of this effort was the requirement that the firing of the shock tube be synchronized with the shock tube oscillation so that the shock wave arrives at the interface at the same point in the oscillation cycle for every experimental run. Nevertheless, a small amount of run-to-run variation existed. The most prominent source of variation in these experiments was the result of a small amount of timing jitter in the mechanical puncturing of the diaphragm which caused the shock wave to arrive at slightly varying times in the oscillation cycle and thus produced slight differences (approximately 10%) in the amplitudes of the initial perturbations. When the initial amplitude is small, as it is in the experiments reported here, these small variations will only result in a change in the initial growth rate as given by (1). Therefore, the approximately 10% variation observed in the initial amplitude will only result in a 10% variation in the rate of

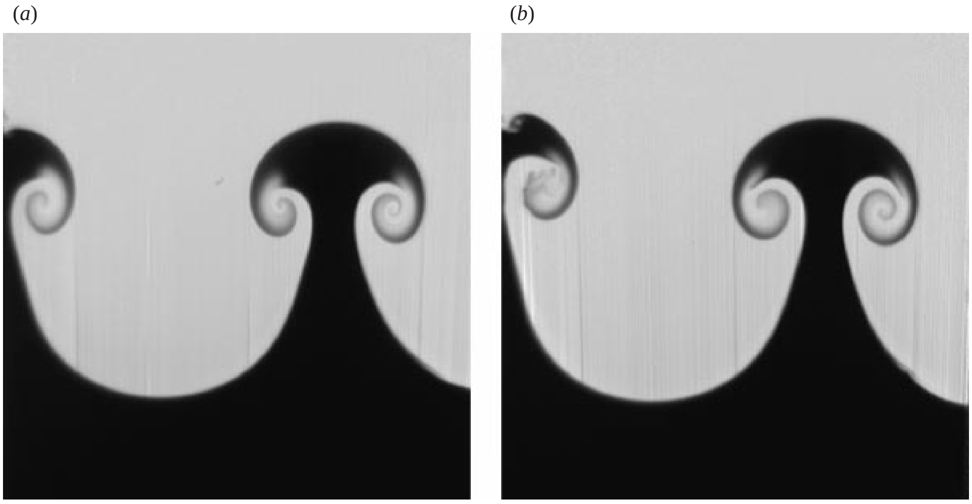

FIGURE 9. A comparison of two images taken at approximately the same time after shock interaction showing the degree of repeatability in the experiments. Both were taken 5.01 ± 0.005 ms after shock acceleration by a $M_s = 1.21$ shock wave. However, the two images appear to have been taken at slightly different times, an outcome that can be attributed to small variations that exist in the initial amplitudes of each run.

development of the instability. This effect is demonstrated in the two images shown in figure 9 which were taken at essentially the same time after shock interaction from two different experiments. The primary difference between the two pictures (which in this case was chosen to be larger than that typically observed) is that they appear to have been taken at slightly different stages in their development. Thus, the primary result of the variation in the initial perturbations in these experiments was to produce slight inconsistency in the apparent age of a particular image. This variation resulted in an equivalent amount of scatter in measurements of the perturbation amplitude described below.

4.2. *Null experiments*

In addition to experiments with single-mode sinusoidal initial perturbations, a small number of experiments were performed with no intentional disturbance (i.e. with a nominally flat initial interface) to determine whether there were appreciable unwanted initial perturbations introduced to the system during the course of an experiment. If the interface is initially perfectly flat then passing a shock wave through it should in theory yield no change and the interface should remain flat for all time. To test the experimental apparatus for the presence of unwanted initial perturbations, which might, for example, be introduced by the method of interface creation, 'null' experiments were performed with the oscillation system turned off. Figure 10 shows the result of one of these null experiments taken at $t = 6.0$ ms with a shock strength of $M_s = 1.11$. Note that, except for the effects of the boundary layers visible along the walls, the interface remains remarkably flat.

4.3. *Amplitude and displacement measurements*

Measurement of the displacement of the post-shock interface is important to quantify the acceleration received by the system. The interface displacement was estimated by averaging the distance travelled by the centremost peak and trough of each image,

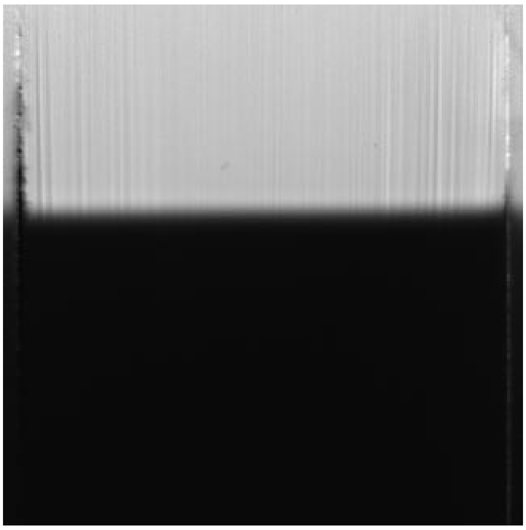

FIGURE 10. An image of an initially unperturbed interface 6.0 ms after it has been impulsively accelerated by a $M_s = 1.11$ shock wave. The interface remains flat, indicating that there is no appreciable initial perturbation produced by the method of interface generation.

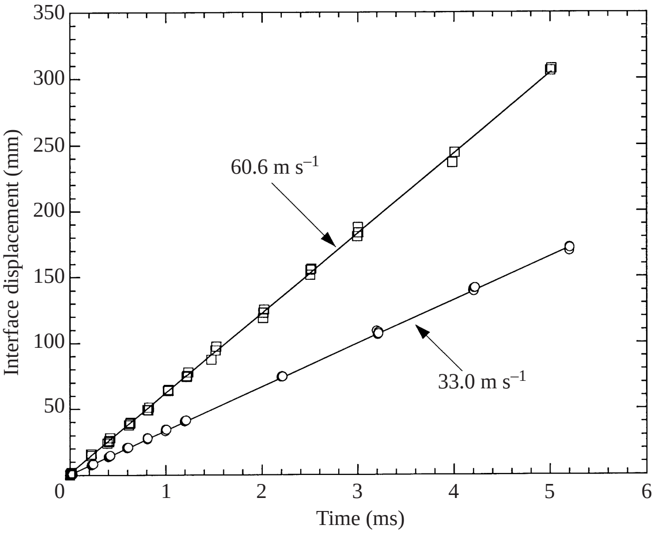

FIGURE 11. Measured interface displacement as a function of time with linear curve fits added to the data: ○, $M_s = 1.11$; □, $M_s = 1.21$.

relative to its initial position in the shock tube. Figure 11 is a plot of the interfacial displacement as a function of time for the $M_s = 1.11$ and the $M_s = 1.21$ experiments. Each curve contains data from approximately 50 separate runs. The data indicate that the interface has a constant velocity up to the time it is reaccelerated by the expansion wave. It is interesting that this is true despite the presence of the two open slots in the test section. Theoretical values for the interface velocities were calculated using a one-dimensional analysis assuming perfect gas behaviour and a non-ventilated shock tube with the measured shock velocities. This calculation yielded an interface velocity of 36.0 m s^{-1} for the $M_s = 1.11$ experiments and 64.2 m s^{-1} for the $M_s = 1.21$

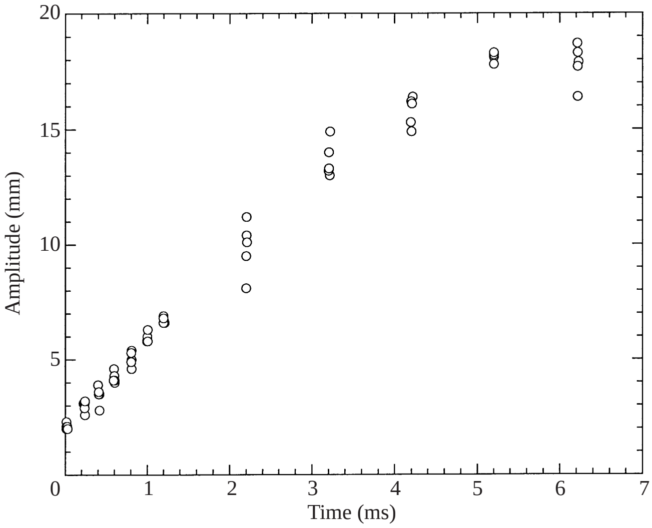

FIGURE 12. Measured amplitude as a function of time for all of the $M_s = 1.11$ experiments.

experiments. Both of these values differ slightly from the experimentally determined values of $33.0\,\mathrm{m\,s^{-1}}$ and $60.6\,\mathrm{m\,s^{-1}}$, found by fitting lines to the data of figure 11. This discrepancy is consistent with the presence of openings (the two slots) in the shock tube.

The interfacial amplitude, defined as half the vertical distance between the top of the centremost crest to the bottom of the centremost trough, is plotted as a function of time for the $M_s = 1.11$ experiments in figure 12. The small amount of scatter observed in this plot can be attributed to the slight variation of the initial perturbation amplitude, as described above. The amplitude as observed in this plot initially grows linearly and begins to deviate from linearity when the amplitude becomes large. The constancy of the early-time growth rate is demonstrated in figure 13 which shows amplitude measurements for the $M_s = 1.11$ experiments where each data point represents an average over 5 measurements. The error bars in this plot signify the 95% confidence intervals based on the statistics of these averages. Also shown on this plot is a line fit to the data indicating a growth rate of $3.92\,\mathrm{m\,s^{-1}}$ with a 95% confidence interval of $\pm 0.23\,\mathrm{m\,s^{-1}}$. The similar measurement for the $M_s = 1.21$ experiments yields a growth rate of $6.28 \pm 0.60\,\mathrm{m\,s^{-1}}$.

For the small initial amplitudes utilized in these experiments (wavenumber × initial amplitude ≈ 0.2), one should expect the initial growth rate, i.e. the slope of the data in the very early portion of figure 12 (up to $t \approx 1$ ms), to be in good agreement with that of linear stability theory. Recall that the instability of an impulsively accelerated incompressible system was considered by Richtmyer (1960) who found the growth rate to be given by (equation (1) in § 1)

$$\frac{\mathrm{d}a}{\mathrm{d}t} = kAVa_0.$$

Richtmyer realized that the Atwood number and initial amplitude would both be altered by the shock wave compression. To determine which amplitudes and Atwood numbers should be used (pre-shock or post-shock), he compared numerical simulations of a shock wave passing from a light to heavy fluid and concluded that

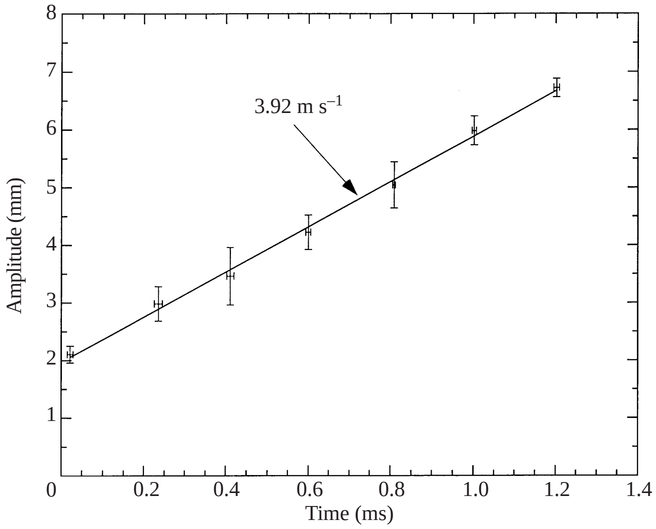

FIGURE 13. Early-time amplitude for the $M_s = 1.11$ experiments. Each data point is an average of measurements from five experiments.

using the post-shock values resulted in the best agreement, with a difference of approximately 10% between computational and theoretical results.

Richtmyer's linear stability solution assumes that the two fluids are separated by a sharp, discontinuous interface, which is not representative of the somewhat diffuse interface created in this experiment. Brouilette & Sturtevant (1994) addressed the instability of a diffuse interface by extending the analysis of the Rayleigh–Taylor instability performed by Duff, Harlow & Hirt (1962) and found the growth rate for a Richtmyer–Meshkov diffuse interface system to be given by,

$$\frac{\mathrm{d}a}{\mathrm{d}t} = \frac{kAV}{\psi} a_0, \tag{6}$$

where ψ is a growth reduction factor that is determined as the eigenvalue of the Sturm–Liouville boundary value problem

$$\left.\begin{aligned} \frac{1}{\rho}\left(\rho\frac{\mathrm{d}f}{\mathrm{d}y}\right) - \left(1 - \frac{\psi}{kA}\frac{1}{\rho}\frac{\mathrm{d}\rho}{\mathrm{d}y}\right)k^2 f = 0, \\ f \to 0 \quad \text{as} \quad y \to \pm\infty. \end{aligned}\right\} \tag{7}$$

Note that $\psi = 1$ corresponds to a discontinuous interface with the value increasing monotonically with increasing interface thickness. Equation (7) was solved numerically assuming an error-function density distribution,

$$\rho = \rho_1 + \frac{\rho_2 - \rho_1}{2}[1 + \mathrm{erf}(\sqrt{\pi}y/\delta)],$$

where the maximum slope thickness δ was estimated by fitting an equivalent expression to the measured tracer concentration distribution in the present experiments. The error-function distribution is a suitable choice because it is the steady-state concentration distribution produced at an interface between two gases experiencing constant normal strain, a condition which approximates the flow field in the vicinity of the interface in the present experiments well. In addition, this distribution provides a good fit to the experimental data. Using the tracer concentration field to evaluate (7) makes

	$M_s = 1.11$		$M_s = 1.21$	
	Pre-shock	Post-shock	Pre-shock	Post-shock
A	0.604	0.616	0.604	0.625
a_0	2.29 mm	2.10 mm	1.83 mm	1.57 mm
ψ	1.204	1.132	1.17	1.08
$\frac{\mathrm{d}a}{\mathrm{d}t}$ (computed)	$4.02\,\mathrm{m\,s^{-1}}$	$3.99\,\mathrm{m\,s^{-1}}$	$6.07\,\mathrm{m\,s^{-1}}$	$5.85\,\mathrm{m\,s^{-1}}$
$\frac{\mathrm{d}a}{\mathrm{d}t}$ (measured)	$3.92\,\mathrm{m\,s^{-1}}$		$6.28\,\mathrm{m\,s^{-1}}$	
Difference	−2.6%	−1.8%	+3.3%	+6.8%

TABLE 1. Parameter values and measurements for the experiments.

the assumption that the presence and concentration of the acetone tracer is equivalent to the presence and concentration of the air–acetone mixture. Unfortunately, this is not entirely accurate because the diffusion coefficients for air into SF_6 and acetone into SF_6 are not the same. The diffusion coefficients of the three binary constituent combinations, air–SF_6, air–acetone and SF_6–acetone, are 0.10, 0.11 and $0.05\,\mathrm{cm^2\,s^{-1}}$, respectively. The relative similarity of these three values, noting that the width of the diffusion zone is proportional to the square root of the diffusivity, supports the use of the measured acetone distribution as an approximation for the density distribution in the integration of (7).

Table 1 contains pre-shock and post-shock values of the Atwood number, the initial perturbation amplitude, and the diffuse-interface correction factor, ψ. The perturbation amplitudes are averaged values measured from PLIF images, and the correction factor was computed as described above. The Atwood number was determined from measured pre-shock gas densities with post-shock values computed from the one-dimensional calculation. These parameter values were used along with the measured interface velocities and wavenumbers to compute pre- and post-shock estimates of the growth rate using the modified form of Richtmyer's formula (6). These computed growth rates are given in table 1 along with the measured values. Note that the theoretical growth rate computed using the post-shock values provides the best estimate for the $M_s = 1.11$ experiments. However, both pre- and post-shock values provide very good agreement with the experimental measurement, differing in the worst case by less than 3%, which is well within the ±6% experimental error estimate. Conversely, the $M_s = 1.21$ results favour the pre-shock values, but again both estimates lie very near the experimental measurement, in this case differing by no more than 7%. It is somewhat unexpected that both of the $M_s = 1.21$ theoretical predictions overestimate the measurement. Nevertheless, the differences are smaller than the ±9.5% error estimate. It is notable that the growth rate estimates obtained using the pre-shock and post-shock parameters yield surprisingly similar values. This occurs because the shock compression decreases both the initial amplitude and the interface thickness. Decreasing the amplitude results in a smaller growth rate, but conversely, a decrease in the interface thickness produces an increase in the growth rate. In this way, the two effects serve to offset each other.

Figure 14 is a plot of dimensionless amplitude relative to its initial value versus a dimensionless time scale defined by the initial growth rate for both the $M_s = 1.11$ and $M_s = 1.21$ experiments. Note that the linear stability theory dictates that the

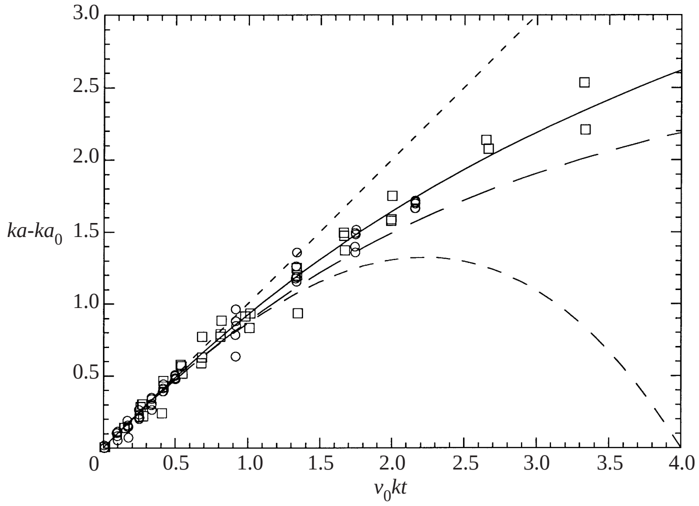

FIGURE 14. Dimensionless amplitude as a function of dimensionless time: ○, $M_s = 1.11$; □, $M_s = 1.21$; ----- , linear theory, equation (6); — — — , Zhang & Sohn (1997), equation (8); ——, Zhang & Sohn (1997), equation (9); —— , Sadot *et al.* (1998), equation (10).

amplitude should grow linearly with time as shown by the straight line in this plot. Thus the curvature present in this amplitude plot is a result of the nonlinearity of the instability. As mentioned above, Zhang & Sohn (1997) and Sadot *et al.* (1998) have developed nonlinear models that they have shown to provide good agreement with both experiments and computation. Zhang & Sohn's result is based on their weakly nonlinear asymptotic solution of the inviscid incompressible instability, which yields

$$v = v_0[1 - (a_0k)v_0kt + (A^2 - \tfrac{1}{2})v_0^2k^2t^2 + O(a_0k)^5], \tag{8}$$

where $v = (v_b + v_s)/2$ is termed the overall growth rate (which is equal to $\mathrm{d}a/\mathrm{d}t$ in the present study), v_0 is its initial value, and $v_{b,s}$ are the individual bubble and spike growth rates. Note that this asymptotic solution has the form of a power series, which must be truncated in order to evaluate the solution. The truncated series yields good agreement with the exact solution for only limited time and diverges very early in the development when the amplitude becomes large, as can be observed in figure 14 which shows (8) truncated at second order. Understanding this difficulty Zhang & Sohn posed their solution in the form of a Padé approximant,

$$v = \frac{v_0}{1 + v_0a_0k^2t + \max\{0, a_0^2k^2 - A^2 + \tfrac{1}{2}\}v_0^2k^2t^2}, \tag{9}$$

which provides a much better behaved solution at late times, as can be observed in figure 14. Even though (9) is based on the solution of the governing equations it lacks the accepted long-time behaviour that the growth rate should decay as $1/t$ (Alon *et al.* 1995; Jacobs & Sheeley 1996) which may explain why it appears to diverge from the data at late times. Sadot *et al.*'s (1998) somewhat more complex model,

$$v_{b/s} = \frac{v_0(1 + v_0kt)}{1 + (1 \pm A)v_0kt + [(1 \pm A)/(1 + A)](1/2\pi C)v_0^2k^2t^2}, \tag{10}$$

captures the desired $1/t$ long-time dependence along with some agreement (up to first order) with the weakly nonlinear solution. However, it contains free parameters which must be determined by comparison with experimental measurements. Sadot *et al.* suggest that $C = 1/3\pi$ for $A > 0.5$ and $C \to 1/2\pi$ when $A \to 0$. They found $C = 1/3\pi$ by analysing the motion of an array of two-dimensional bubbles of negligible density (i.e. $A = 1$), and $C = 1/2\pi$ by modelling RM instability in a nearly uniform density distribution (i.e. $A = 0$) by assuming that the flow field is that of a row of line vortices (Jacobs & Sheeley 1996). Thus the correct value of C for intermediate Atwood numbers is uncertain. Following the suggestion of Sadot *et al.*, we use $C = 1/3\pi$ for our Atwood number of 0.6. Note that (10) provides separate bubble and spike growth rates, where the plus sign is used for the bubble velocity and the minus for the spike. Thus the overall velocity is given by $v = (v_b + v_s)/2$. Figure 14 also shows a curve corresponding to Sadot *et al.*'s model (10), which provides the best fit of the experimental data. Thus the $1/t$ dependence appears to be a necessary ingredient to achieve good late-time agreement.

5. Conclusions

Use of the novel method for interface generation developed by Jones & Jacobs (1997) enables advanced visualization techniques, such as PLIF imaging, of the Richtmyer–Meshkov instability in a shock tube environment. In this study PLIF images have been captured of the developing instability from the initial sinusoidal perturbation stage, through the nonlinear growth regime, and into turbulence. The quality and reproducibility of the images provided by this technique are well beyond that of all previous single-interface RM experiments, and reveal for the first time details of the RM instability in a shock tube environment, such as the secondary instability of the vortex cores and the small-scale features resulting from reacceleration by the reflected shock and expansion waves.

Early-time measurements of the growth rate are in good agreement with Richtmyer's (1960) incompressible model when combined with Brouillette & Sturtevant's (1994) diffuse-interface correction. The experimental results differ from the theoretical model by less than 7% in the $M_s = 1.21$ case, and by less than 3% in the $M_s = 1.11$ experiments. In addition, very good agreement is also attained with the nonlinear models of Zhang & Sohn (1997) and Sadot *et al.* (1998). The model of Sadot *et al.* (1998) agrees best with the data owing to the fact that it captures the generally accepted $1/t$ behaviour of the growth rate at late times. However, it suffers from the fact that it is at least partially empirical in that it contains parameters that must be extracted from experiments or calculations.

Comparison of images from the $M_s = 1.11$ and $M_s = 1.21$ sequences reveal a significant increase in the amount of mixed fluid in the higher Mach number experiments, suggesting that a mixing transition, similar to that observed in other shear flows, has occurred. However, because the turbulence in this case is produced as a result of interaction with both reflected shock and expansion waves the conditions necessary for this transition to occur are difficult to quantify. Note that an appropriate Reynolds number is difficult to define in this case because the complexity of both the interface and the acceleration history precludes the determination of appropriate length and velocity scales.

The authors wish to thank Dr Vitaliy Krivets for his help in constructing the wave diagrams. This research was supported by Lawrence Livermore National Laboratory and by NASA's Microgravity Fluid Physics Program.

REFERENCES

Aleshin, A. N., Gamalii, E. G., Zaitsev, S. G., Lazareva, E. V., Lebo, I. G. & Rozanov, V. B. 1988 Nonlinear and transitional states in the onset of the Richtmyer–Meshkov instability. *Sov. Tech. Phys. Lett.* **14** (6), 466–468 (transl. of *Pis'ma Zh. Tekh. Fiz.* **14**, 1063–1067).

Alon, U., Hecht, J., Ofer, D. & Shvarts, D. 1995 Power laws and similarity of Rayleigh–Taylor and Richtmyer–Meshkov mixing fronts at all density ratios. *Phys. Rev. Lett.* **74**, 534–537.

Arnett, W. D., Bahcall, J. N., Kirshner, R. P. & Woosley, S. E. 1989 Supernova 1987A. *Annu. Rev. Astron. Astrophys.* **27**, 629–700.

Benjamin, R. F. 1992 Experimental observations of shock stability and shock-induced turbulence. In *Advances in Compressible Turbulent Mixing, Proc. First Intl Workshop on the Physics of Compressible Turbulent Mixing* (ed. W. P. Dannevik, A. C. Buckingham & C. E. Leith), pp. 341–348. Lawrence Livermore National Laboratory, Conf-8810234.

Bonazza, R. & Sturtevant, B. 1996 X-ray measurements of growth rates at a gas interface accelerated by shock waves. *Phys. Fluids* **8**, 2496–2512.

Breidenthal, R. E. 1981 Structure in turbulent mixing layers and wakes using a chemical reaction. *J. Fluid Mech* **109**, 1–24.

Brouilette, M. & Sturtevant, B. 1994 Experiments on the Richtmyer–Meshkov instability: single-scale perturbations on a continuous interface. *J. Fluid Mech.* **263**, 271–292.

Budzinski, J. M., Benjamin, R. F. & Jacobs, J. W. 1994 Influence of initial conditions on the flow patterns of a shock-accelerated thin fluid layer. *Phys. Fluids* **6**, 3510–3512.

Cavailler, C., Mercier, P., Rodriguez, G. & Haas, J. F. 1990 A new vertical shock tube for Rayleigh–Taylor instability measurements. *Proc. 17th ISSWST at Bethlehem PA; Current Topics in Shock Waves* (ed. Y. Kim), p. 564. American Institute of Physics.

Dimotakis, P. E. 2000 The mixing transition in turbulent flows. *J. Fluid Mech.* **409**, 69–97.

Duff, R. E., Harlow, F. H. & Hirt, C. W. 1962 Effects of diffusion on interface instability between gases. *Phys. Fluids* **5**, 417–425.

Haan, S. W. 1991 Weakly nonlinear hydrodynamic instabilities in inertial fusion. *Phys. Fluids* B **3**, 2349–2355.

Jacobs, J. W. 1993 The dynamics of shock accelerated light and heavy gas cylinders. *Phys. Fluids* A **5**, 2239–2247.

Jacobs, J. W., Jenkins, D. G., Klein, D. L. & Benjamin, R. F. 1995 Nonlinear growth of the shock-accelerated instability of a thin fluid layer. *J. Fluid Mech.* **295**, 23–42.

Jacobs, J. W., Klein, D. L., Jenkins, D. L. & Benjamin, R. F. 1993 Instability growth patterns of a shock-accelerated thin fluid layer. *Phys. Rev. Lett.* **70**, 583–586.

Jacobs, J. W. & Niederhaus, C. E. 1997 PLIF flow visualization of single and multi-mode incompressible Richtmyer–Meshkov instability. In *Proc. 6th Intl Workshop on the Physics of Compressible Turbulent Mixing, Marseille, France* (ed. G. Jourdan & L. Houas). Universite de Provence.

Jacobs, J. W. & Sheeley, J. M. 1996 Experimental study of incompressible Richtmyer–Meshkov instability. *Phys. Fluids* **8**, 405–415.

Jones, M. A. & Jacobs, J. W. 1997 A membraneless experiment for the study of Richtmyer–Meshkov instability of a shock-accelerated gas interface. *Phys. Fluids* **9**, 3078–3085.

Koochesfahani, M. M. & Dimotakis, P. E. 1986 Mixing and chemical reactions in a turbulent liquid mixing layer. *J. Fluid Mech.* **170**, 83–112.

Kotelnikov, A. D., Ray, J. & Zabusky, N. J. 2000 Vortex morphologies on reaccelerated interfaces: Visualization, quantification and modeling of one- and two-mode compressible and incompressible environments. *Phys. Fluids* **12**, 3245–3264.

Lindl, J. D., McCrory, R. L. & Campbell, E. M. 1992 Progress toward ignition and burn propagation in inertial confinement fusion. *Physics Today* **45** (9), 32–50.

Lozano, A., Yip, B. & Hanson, R. K. 1992 Acetone: A tracer for concentration measurements in gaseous flows by planar laser-induced fluorescence. *Exps. Fluids* **13**, 369–376.

Meshkov, E. E. 1969 Instability of the interface of two gases accelerated by a shock wave. *Izv. Akad. Nauk. SSSR Mekh. Zhidk. Gaza.* **4**, 151–157. (transl. of *Izv. Acad. Sci. USSR Fluid Dyn.* **4**, 101–104).

Niederhaus, C. E. 2000 Experiments on the Richtmyer–Meshkov instability of incompressible fluids. PhD dissertation, University of Arizona.

Rayleigh, Lord 1883 Investigation of the character of the equilibrium of an incompressible heavy fluid of variable density. *Proc. Lond. Math. Soc.* **14**, 170–177. (Reprinted in *The Scientific Papers of Lord Rayleigh*, vol. II, p. 200. Cambridge University Press, 1900.)

Richtmyer, R. D. 1960 Taylor instability in shock acceleration of compressible fluids. *Commun. Pure Appl. Maths* **23**, 297–319.

Rightley, P. M., Vorobieff, R., Martin, R. & Benjamin, R. F. 1999 Experimental observations of the mixing transition in a shock-accelerated gas curtain. *Phys. Fluids* **11**, 186–200.

Sadot, O., Erez, L., Alon, U., Oron, D., Levin, L. A., Erez, G., Ben-Dor, G. & Shvarts, D. 1998 Study of nonlinear evolution of single-mode and two-bubble interaction under Richtmyer–Meshkov instability. *Phys. Rev. Lett.* **80**, 1654–1657.

Taylor, G. I. 1950 The instability of liquid surfaces when accelerated in a direction perpendicular to their planes. I. *Proc. Roy. Soc. Lond.* A **201**, 192–196.

Vassilenko, A. M., Buryakov, O. V., Kuropatenko, V. F., Olkhovskaya, V. I., Ratnikov, V. P. & Jakovlev, V. G. 1992 Experimental research of gravitational instability and turbulization of flow at the noble gases interface. In *Advances in Compressible Turbulent Mixing, First Intl Workshop on the Physics of Compressible Turbulent Mixing* (ed. W. P. Dannevik, A. C. Buckingham & C. E. Leith), pp. 581–606. Lawrence Livermore National Laboratory, Conf-8810234.

Waddell, J. T., Niederhaus, C. E. & Jacobs, J. W. 2001 Experimental study of Rayleigh–Taylor instability: Low Atwood number liquid systems with single-mode initial perturbations. *Phys. Fluids* **13**, 1263–1273.

Yang, J., Kubota, T. & Zukoski, E. E. 1993 Application of shock induced-mixing to supersonic combustion. *AIAA J.* **31**, 854–862.

Zabusky, N. J. 1999 Vortex Paradigm for accelerated inhomogeneous flows: Visiometrics for the Rayleigh–Taylor and Richtmyer–Meshkov environments. *Annu. Rev. Fluid Mech.* **31**, 495–536.

Zhang, Q. & Sohn, S. 1997 Non-linear theory of unstable fluid mixing driven by shock wave. *Phys. Fluids* **9**, 1106–1124.